Bifurcation and chaos analysis for aeroelastic airfoil with freeplay structural nonlinearity in pitch*

Zhao De-Min(赵德敏) and Zhang Qi-Chang(张琪昌)†

Department of Mechanics, School of Mechanical Engineering, Tianjin University, Tianjin 300072, *China*
State Key Laboratory of Engines, Tianjin University, Tianjin 300072, *China*

(Received 13 April 2009; revised manuscript received 24 September 2009)

The dynamics character of a two degree-of-freedom aeroelastic airfoil with combined freeplay and cubic stiffness nonlinearities in pitch submitted to supersonic and hypersonic flow has been gaining significant attention. The Poincaré mapping method and Floquet theory are adopted to analyse the limit cycle oscillation flutter and chaotic motion of this system. The result shows that the limit cycle oscillation flutter can be accurately predicted by the Floquet multiplier. The phase trajectories of both the pitch and plunge motion are obtained and the results show that the plunge motion is much more complex than the pitch motion. It is also proved that initial conditions have important influences on the dynamics character of the airfoil system. In a certain range of airspeed and with the same system parameters, the stable limit cycle oscillation, chaotic and multi-periodic motions can be detected under different initial conditions. The figure of the Poincaré section also approves the previous conclusion.

Keywords: airfoil flutter, bifurcation and chaos, freeplay nonlinearity, Poincaré map
PACC: 0547, 4740K, 4660D

1. Introduction

Recently the aeroelastic analysis of aircraft structures is often assumed that both the aeroedynamic and structural forces are nonlinear when airspeed increases to subsonic or transonic Mach numbers, because many experiments, whether performed in a wind tunnel or in flight, have shown that many phenomena are capable of being predicted from the nonlinear dynamics. In an airfoil system, three types of concentrated structural nonlinearities, namely cubic, freeplay and hysteresis stiffnesses have significant effects on the aeroelastic responses of the airfoil surfaces.[1]

Up to now, theoretical and numerical studies[2−6] have been widely performed using the centre manifold theory and the normal form method or harmonic balance method on the cubic structural nonlinearities airfoil systems. Some other investigations were conducted for the aircraft aeroelastic system with freeplay nonlinearities. Reference [7] investigated a two-dimensional aeroelastic system model with freeplay using a point transformation technique. In Refs. [8] and [9], the bifurcation of a two-degree-of-freedom (2-DOF) aeroelastic system with freeplay and hysteresis structural nonlinearity was investigated by a perturbation-incremental method. In Refs. [10]–[13] a two-dimensional airfoil with control surface freeplay nonlinearity was investigated completely and the flutter suppression technique was proposed successfully employing the ultrasonic motor. The flutter margin estimation was studied using a modern robust flutter method in Refs. [14]. Reference [15] numerically studied the flutter and post flutter of a two-dimensional double-wedge lifting surface with combined freeplay and cubic stiffness nonlinearities in both plunge and pitch DOF.

It is well known that the mathematic model of the system with freeplay and cubic stiffness combined nonlinearities exhibits a piecewise-smooth nonlinear dynamical system. This system has complexity[16] and can be investigated comprehensively based on the Poincaré map method.[17−20] Although, Refs. [7]–[9] introduced the point transformation and perturbation-incremental methods to study the aircraft system with freeplay stiffness, these methods are used successfully in piecewise-smooth linear aeroelastic airfoil systems rather than in nonlinear ones. To overcome these drawbacks, the Poincaré

*Project supported by the National Natural Science Foundation of China (Grant No. 10872141), the Research Fund for the Doctoral Program of Higher Education (Grant No. 20060056005) and the National Basic Research Program of China (Grant No. 007CB714000).
†Corresponding author. E-mail: qzhang@tju.edu.cn
© 2010 Chinese Physical Society and IOP Publishing Ltd

map method is used to study the aircraft system with piecewise-nonlinearity which combined freeplay and cubic nonlinearities. Briefly, the aim of this paper is to demonstrate more profoundly the limit cycle flutter and chaos of a 2-DOF airfoil with combined freeplay and cubic stiffness nonlinearities submitted supersonic and hypersonic flow.

2. Aeroelastic mathematical model

Considered a 2-DOF wedge aerofoil oscillating in pitch and plunge as shown in Fig. 1.

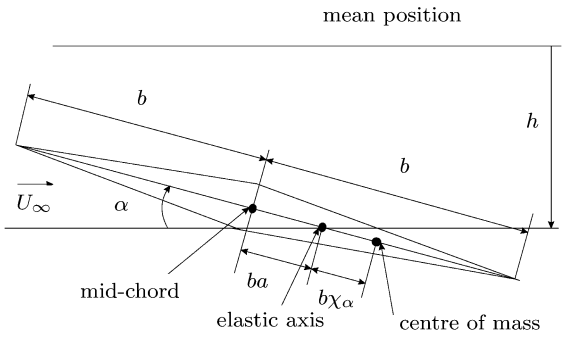


Fig. 1. The sketch of a 2-DOF airfoil motion.

The basic structural dynamics model is obtained in Refs. [1] and [15]. The 2-DOF dynamic aeroelastic equations for the pitch and plunge motion with combined freeplay and cubic stiffness nonlinearities in pitch can be expressed as follows:

$$S_\alpha \ddot{h} + I_\alpha \ddot{\alpha} + c_\alpha \dot{\alpha} + G(\alpha) = M_{\rm EA}(t), \tag{1a}$$

$$m\ddot{h} + S_\alpha \ddot{\alpha} + c_h \dot{h} + K_h h = -\bar{L}(t), \tag{1b}$$

where the plunge displacement is denoted by h and the pitch angle is α; the dots denote differentiation with respect to time; where the symbols m, S_α, c_h , I_α and c_α are the airfoil mass, airfoil static moment about the elastic axis, damping coefficient in plunge, wing mass moment of inertia about elastic axis, and torsion damping constant, respectively; $G(\alpha)$ is utilized to describe the structural nonlinearity represented by coupled freeplay and cubic stiffness nonlinearities in pitch; the function curve of the moment $G(\alpha)$ versus displacement α is shown in Fig. 2, which can also be described as follows:[15]

$$G(\alpha) = G_a(\alpha) + G_b(\alpha) + G_c(\alpha), \tag{2}$$

where

$$G_a(\alpha) = \begin{cases} K_\alpha \alpha, & \alpha > \alpha_s; \\ 0, & -\alpha_s \le \alpha \le \alpha_s \ ; \\ K_\alpha \alpha, & \alpha < -\alpha_s; \end{cases}$$

$$G_b(\alpha) = \begin{cases} -K_\alpha \alpha_s, & \alpha > \alpha_s; \\ 0, & -\alpha_s \le \alpha \le \alpha_s; \\ K_\alpha \alpha_s, & \alpha < -\alpha_s; \end{cases}$$

$$G_c(\alpha) = \begin{cases} \hat{K}_\alpha (\alpha - \alpha_s)^3, & \alpha > \alpha_s; \\ 0, & -\alpha_s \le \alpha \le \alpha_s; \\ \hat{K}_\alpha (\alpha + \alpha_s)^3, & \alpha < -\alpha_s. \end{cases}$$

In Eq.(1), $L(t)$ and $M_{\rm EA}(t)$ are the nonlinear aerodynamic loads named the lift force and aerodynamic moment respectively, which are derived from a third-order expansion form of the piston theory aerodynamics (PTA).[15]

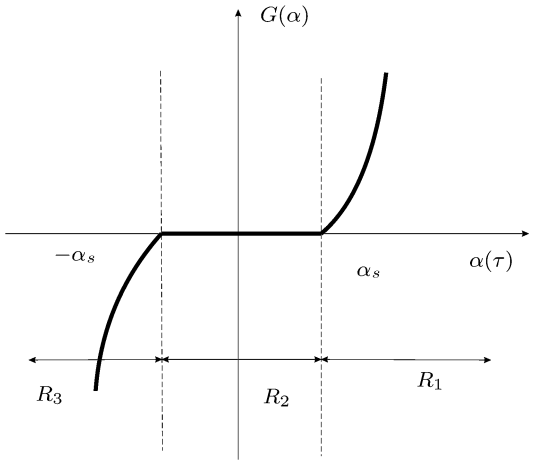


Fig. 2. General sketch of combined freeplay and cubic stiffness nonlinearities model in pitch.

Equations (1) can be rewritten as equation (3)[15] by introduce non-dimensional transformation as shown in Appendix A.

$$\begin{bmatrix} 1 & \frac{\chi_\alpha}{r_\alpha^2} \\ \chi_\alpha & 1 \end{bmatrix} \begin{bmatrix} \alpha''(\tau) \\ \xi''(\tau) \end{bmatrix} + \begin{bmatrix} c_{11} & c_{12} \\ c_{21} & c_{22} \end{bmatrix} \begin{bmatrix} \alpha'(\tau) \\ \xi'(\tau) \end{bmatrix} + \begin{bmatrix} k_{11} & k_{12} \\ k_{21} & k_{22} \end{bmatrix} \begin{bmatrix} \alpha \\ \xi \end{bmatrix} + \begin{bmatrix} \bar{f}_1 \\ \bar{f}_2 \end{bmatrix} = \begin{bmatrix} 0 \\ 0 \end{bmatrix}. \tag{3}$$

Select the state variable $\boldsymbol{X}$ as $\boldsymbol{X} = \{\alpha\ \alpha'\ \xi\ \xi'\} = \{x_1\ x_2\ x_3\ x_4\}^{\mathrm{T}}$. The Eq. (3) can be transformed into the following first-order ordinary differential equations (ODEs):

$$\boldsymbol{X}' = \begin{bmatrix} 0 & 1 & 0 & 0 \\ a_{21} & a_{22} & a_{23} & a_{24} \\ 0 & 0 & 0 & 1 \\ a_{41} & a_{42} & a_{43} & a_{44} \end{bmatrix} \boldsymbol{X} + \begin{bmatrix} 0 \\ f_1 \\ 0 \\ f_2 \end{bmatrix} = \begin{bmatrix} F_1(\boldsymbol{X}) \\ F_2(\boldsymbol{X}) \\ F_3(\boldsymbol{X}) \\ F_4(\boldsymbol{X}) \end{bmatrix}, \tag{4}$$

where $c_{11},\ c_{12},\ c_{21},\ c_{22},\ k_{11},\ k_{12},\ k_{21},\ k_{22},\ a_{21},\ a_{22},\ a_{23},\ a_{24},\ a_{41},\ a_{42},\ a_{43},\ a_{44},\ f_1,\ f_2,\ \bar{f}_1,\ \bar{f}_2$ are related to the system parameters and their expressions are given in Appendix B.

Considering the three branches of the freeplay and cubic nonlinear model, the phase space $\boldsymbol{X} \in R^4$ can be divided into three regions $\boldsymbol{R}_1,\ \boldsymbol{R}_2,\ \boldsymbol{R}_3$ as shown in Fig. 3, where the corresponding expressions of the differential equations are given by

$$\begin{aligned} &\boldsymbol{X}' = \boldsymbol{A}_3\boldsymbol{X} + \boldsymbol{B}_3 \quad \text{in} \quad \boldsymbol{R}_3 = \{\boldsymbol{X} \in \mathrm{R}^4 \,|x_1 < -\alpha_s\}, \\ &\boldsymbol{X}' = \boldsymbol{A}_2\boldsymbol{X} + \boldsymbol{B}_2 \quad \text{in} \quad \boldsymbol{R}_2 = \{\boldsymbol{X} \in \mathrm{R}^4 \,|-\alpha_s \le x_1 \le \alpha_s\}, \\ &\boldsymbol{X}' = \boldsymbol{A}_1\boldsymbol{X} + \boldsymbol{B}_1 \quad \text{in} \quad \boldsymbol{R}_1 = \{\boldsymbol{X} \in \mathrm{R}^4 \,|x_1 > \alpha_s\}. \end{aligned} \tag{5}$$

Here $\boldsymbol{A}_i$ is a 4×4 constant matrix, and $\boldsymbol{B}_i$ is a 4×1 constant vector.

3. The Poincaré map method

Consider the freeplay nonlinear model shown in Fig. 2. Let the $\boldsymbol{Z} - \boldsymbol{Y}$ plane represent a four-dimensional phase space, where $\boldsymbol{Z} = \{\alpha\} = \{y_1\}$ and $\boldsymbol{Y} = \{\alpha', \xi, \xi'\}^{\mathrm{T}} = \{y_2, y_3, y_4\}^{\mathrm{T}}$. The $\boldsymbol{Z} - \boldsymbol{Y}$ phase space is now divided into three region $\boldsymbol{R}_1$, $\boldsymbol{R}_2$, $\boldsymbol{R}_3$ respectively by $x_1 = \alpha_s$ and $x_1 = -\alpha_s$. We define two hyperplanes $\boldsymbol{\Pi}_0 = \{\alpha, \alpha', \xi, \xi')\,|\alpha = \alpha_s\}$ and $\boldsymbol{\Pi}_1 = \{\alpha, \alpha', \xi, \xi')\,|\alpha = -\alpha_s\}$ as the Poincaré sections with $\boldsymbol{\pi}_0$ and $\boldsymbol{\pi}_1$, expressed by $\boldsymbol{\pi}_0 = \boldsymbol{\pi}_1 = (1, 0, 0, 0)$, being the direction of $\boldsymbol{\Pi}_0$ and $\boldsymbol{\Pi}_1$ respectively . The system response then can be predicted by following a general phase path shown in Fig. 3. Suppose that a motion initially starts from $\boldsymbol{\Pi}_0$ at $\boldsymbol{X}_0$, it passes through $\boldsymbol{R}_1$ and $\boldsymbol{\Pi}_0$ into $\boldsymbol{R}_2$, then crosses the section $\boldsymbol{\Pi}_1$ into $\boldsymbol{R}_3$. Next, it leaves $\boldsymbol{R}_3$ and $\boldsymbol{\Pi}_1$ into $\boldsymbol{R}_2$ again. Finally, the trajectory returns back to $\boldsymbol{\Pi}_0$. The point $\boldsymbol{X}_i$ is called switching point, which can be denoted as follows:

$$\begin{aligned} &\boldsymbol{Z}_i = \{\alpha_i\} = \{y_{1i}\}, \\ &\boldsymbol{Y}_i = \{\alpha_i', \xi_i, \xi_i'\}^{\mathrm{T}} = \{y_{2i}, y_{3i}, y_{4i}\}^{\mathrm{T}}, \\ &\boldsymbol{X}_i = \{\boldsymbol{Z}_i, \boldsymbol{Y}_i\} = \{y_{1i}, y_{2i}, y_{3i}, y_{4i}\}^{\mathrm{T}}, \quad (i = 0, 1, 2, 3, 4). \end{aligned}$$

Note that the following form have used for sake of the explicit expression:

$()_{ji}$,the first subscript j denotes the j dimension of the vector$\{y_1\ y_2\ y_3\ y_4\}^{\mathrm{T}}$, and the second subscript i denotes i switch point.

Based on the above definition, let $\boldsymbol{X}_0$ and $\boldsymbol{X}_1$ be the points through which the trajectory enters $\boldsymbol{R}_1$ and $\boldsymbol{R}_2$ respectively. Let $\boldsymbol{X}_2$ and $\boldsymbol{X}_3$ be the points through which the trajectory leaves $\boldsymbol{R}_2$ and $\boldsymbol{R}_3$ respectively. Denote $\boldsymbol{X}_4$ as the final point of the trajectory which travels one period and then back to $\boldsymbol{\Pi}_0$ as shown in Fig. 3. In all the figures of the whole paper, the hollow circle and diamond signs represent the switch point $\boldsymbol{X}_0$ and $\boldsymbol{X}_1$ respectively, and the square and pentagram signs represent the $\boldsymbol{X}_2$ and $\boldsymbol{X}_3$ respectively.

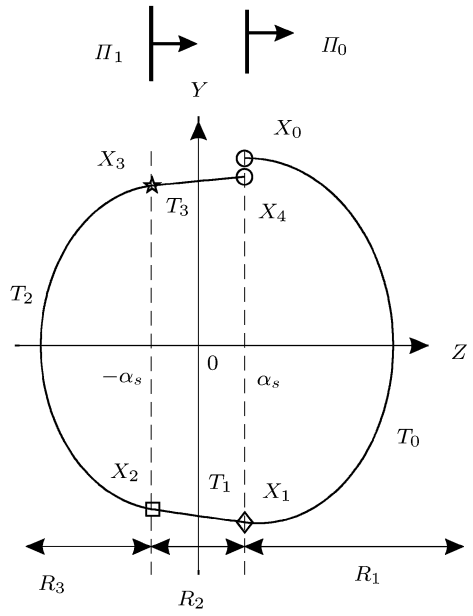


Fig. 3. General trajectory of system with a coupled freeplay and cubic nonlinearities.

Each switching point $\boldsymbol{X}_i$ $(i = 0, 1, 2, 3, 4)$ is a solution function of the previous point such as

$$\boldsymbol{X}_{i+1} = \boldsymbol{\Phi}_i(\boldsymbol{X}_i, \tau_i) \Leftrightarrow \begin{cases} y_{1(i+1)} = \phi_{1i}(y_{1i}, y_{2i}, y_{3i}, y_{4i}, \tau_i), \\ y_{2(i+1)} = \phi_{2i}(y_{1i}, y_{2i}, y_{3i}, y_{4i}, \tau_i), \\ y_{3(i+1)} = \phi_{3i}(y_{1i}, y_{2i}, y_{3i}, y_{4i}, \tau_i), \\ y_{4(i+1)} = \phi_{4i}(y_{1i}, y_{2i}, y_{3i}, y_{4i}, \tau_i), \end{cases} \quad (i = 0, 1, 2, 3). \tag{6}$$

The Poincaré map of every step is expressed as,[21]

$$\boldsymbol{T}_i : \boldsymbol{X}_i \mapsto \boldsymbol{X}_{i+1} = \boldsymbol{\Phi}_i(\boldsymbol{X}_i, \tau_i), \quad i = 0, 1, 2, 3. \tag{7}$$

We now perform a local analysis on each partial orbit delimited by those Poincaré sections. Thus the Poincaré map of the whole state space is defined as a differentiable map

$$\begin{aligned} &\boldsymbol{T} = \boldsymbol{T}_3 \circ \boldsymbol{T}_2 \circ \boldsymbol{T}_1 \circ \boldsymbol{T}_0 : \boldsymbol{X}_0 \to \boldsymbol{X}_4 \\ &y_{20} \mapsto y_{24} = \phi_2(y_{20}, y_{30}, y_{40}, \tau), \\ &y_{30} \mapsto y_{34} = \phi_3(y_{20}, y_{30}, y_{40}, \tau), \\ &y_{40} \mapsto y_{44} = \phi_4(y_{20}, y_{30}, y_{40}, \tau). \end{aligned} \tag{8}$$

For the fixed point of the Poincaré map corresponding to the periodic solution of the system, we require to solve

$$\boldsymbol{T}(\boldsymbol{X}_0) = \boldsymbol{X}_4 = \boldsymbol{X}_0. \tag{9}$$

The Jacobian matrix of the Poincaré map is expressed as follows:

$$\boldsymbol{DT} = \frac{\partial \boldsymbol{Y}_4}{\partial \boldsymbol{Y}_0} = \frac{\partial \boldsymbol{Y}_4}{\partial \boldsymbol{Y}_3}\frac{\partial \boldsymbol{Y}_3}{\partial \boldsymbol{Y}_2}\frac{\partial \boldsymbol{Y}_2}{\partial \boldsymbol{Y}_1}\frac{\partial \boldsymbol{Y}_1}{\partial \boldsymbol{Y}_0}. \tag{10}$$

For each state i, we carry out following computations:

$$\frac{\partial \boldsymbol{Y}_i}{\partial \boldsymbol{Y}_{i-1}} = \begin{bmatrix} \dfrac{\partial \phi_{2i}}{\partial y_{2(i-1)}} - \dfrac{F_2(\boldsymbol{Z}_i, \boldsymbol{Y}_i)}{F_1(\boldsymbol{Z}_i, \boldsymbol{Y}_i)}\dfrac{\partial \phi_{1i}}{\partial y_{2(i-1)}} & \dfrac{\partial \phi_{2i}}{\partial y_{3(i-1)}} - \dfrac{F_2(\boldsymbol{Z}_i, \boldsymbol{Y}_i)}{F_1(\boldsymbol{Z}_i, \boldsymbol{Y}_i)}\dfrac{\partial \phi_{1i}}{\partial y_{3(i-1)}} & \dfrac{\partial \phi_{2i}}{\partial y_{4(i-1)}} - \dfrac{F_2(\boldsymbol{Z}_i, \boldsymbol{Y}_i)}{F_1(\boldsymbol{Z}_i, \boldsymbol{Y}_i)}\dfrac{\partial \phi_{1i}}{\partial y_{4(i-1)}} \\ \dfrac{\partial \phi_{3i}}{\partial y_{2(i-1)}} - \dfrac{F_3(\boldsymbol{Z}_i, \boldsymbol{Y}_i)}{F_1(\boldsymbol{Z}_i, \boldsymbol{Y}_i)}\dfrac{\partial \phi_{1i}}{\partial y_{2(i-1)}} & \dfrac{\partial \phi_{3i}}{\partial y_{3(i-1)}} - \dfrac{F_3(\boldsymbol{Z}_i, \boldsymbol{Y}_i)}{F_1(\boldsymbol{Z}_i, \boldsymbol{Y}_i)}\dfrac{\partial \phi_{1i}}{\partial y_{3(i-1)}} & \dfrac{\partial \phi_{3i}}{\partial y_{4(i-1)}} - \dfrac{F_3(\boldsymbol{Z}_i, \boldsymbol{Y}_i)}{F_1(\boldsymbol{Z}_i, \boldsymbol{Y}_i)}\dfrac{\partial \phi_{1i}}{\partial y_{4(i-1)}} \\ \dfrac{\partial \phi_{4i}}{\partial y_{2(i-1)}} - \dfrac{F_4(\boldsymbol{Z}_i, \boldsymbol{Y}_i)}{F_1(\boldsymbol{Z}_i, \boldsymbol{Y}_i)}\dfrac{\partial \phi_{1i}}{\partial y_{2(i-1)}} & \dfrac{\partial \phi_{4i}}{\partial y_{3(i-1)}} - \dfrac{F_3(\boldsymbol{Z}_i, \boldsymbol{Y}_i)}{F_1(\boldsymbol{Z}_i, \boldsymbol{Y}_i)}\dfrac{\partial \phi_{1i}}{\partial y_{3(i-1)}} & \dfrac{\partial \phi_{4i}}{\partial y_{4(i-1)}} - \dfrac{F_3(\boldsymbol{Z}_i, \boldsymbol{Y}_i)}{F_1(\boldsymbol{Z}_i, \boldsymbol{Y}_i)}\dfrac{\partial \phi_{1i}}{\partial y_{4(i-1)}} \end{bmatrix}, \tag{11}$$

$$\frac{\mathrm{d}}{\mathrm{d}t}\begin{bmatrix} \dfrac{\partial \phi_{1i}}{\partial y_{j(i-1)}} \\ \dfrac{\partial \phi_{2i}}{\partial y_{j(i-1)}} \\ \dfrac{\partial \phi_{3i}}{\partial y_{j(i-1)}} \\ \dfrac{\partial \phi_{4i}}{\partial y_{j(i-1)}} \end{bmatrix} = \begin{bmatrix} \dfrac{\partial F_1}{\partial y_1} & \dfrac{\partial F_1}{\partial y_2} & \dfrac{\partial F_1}{\partial y_3} & \dfrac{\partial F_1}{\partial y_4} \\ \dfrac{\partial F_2}{\partial y_1} & \dfrac{\partial F_2}{\partial y_2} & \dfrac{\partial F_2}{\partial y_3} & \dfrac{\partial F_2}{\partial y_4} \\ \dfrac{\partial F_3}{\partial y_1} & \dfrac{\partial F_3}{\partial y_2} & \dfrac{\partial F_3}{\partial y_3} & \dfrac{\partial F_3}{\partial y_4} \\ \dfrac{\partial F_4}{\partial y_1} & \dfrac{\partial F_4}{\partial y_2} & \dfrac{\partial F_4}{\partial y_3} & \dfrac{\partial F_4}{\partial y_4} \end{bmatrix} \begin{bmatrix} \dfrac{\partial \phi_{1i}}{\partial y_{j(i-1)}} \\ \dfrac{\partial \phi_{2i}}{\partial y_{j(i-1)}} \\ \dfrac{\partial \phi_{3i}}{\partial y_{j(i-1)}} \\ \dfrac{\partial \phi_{4i}}{\partial y_{j(i-1)}} \end{bmatrix}, \quad (j = 2, 3, 4). \tag{12}$$

Appling Eq. (12) for $j = 2, 3, 4$, three matrix equations obtained are labeled as (12a), (12b) and (12c) respectively. We solve simultaneously Eqs. (5), (12a), (12b) and (12c), which yields I as the initial condition. Then we can obtain $\dfrac{\partial \boldsymbol{Y}_i}{\partial \boldsymbol{Y}_{i-1}}$. Substituting Eq. (11) into Eq. (10), we obtain Jacobian $\boldsymbol{DT}$.

By using the Newton–Raphson algorithm to compute the fix point, the Newton–Raphson iterations can be expressed as

$$\begin{bmatrix} \boldsymbol{\alpha}_s^{(m+1)} \\ \boldsymbol{Y}_0^{(m+1)} \end{bmatrix} = \begin{bmatrix} \boldsymbol{\alpha}_s^{(m)} \\ \boldsymbol{Y}_0^{(m)} - \dfrac{\boldsymbol{Y}_4^{(m)} - \boldsymbol{Y}_0^{(m)}}{\boldsymbol{DT}^{(m)} - \boldsymbol{I}} \end{bmatrix}, \tag{13}$$

where $\boldsymbol{I}$ is a three-order identity matrix.

4. Numerical simulation and discussions

The system parameters selected can refer to Ref. [15]. Throughout the paper, the value of the parameters are chosen as: $\chi_\alpha = 0.25$, $r_\alpha = 0.5$, $\xi_h = 0$, $\xi_\alpha = 0$, $\eta = 1$, $\gamma = 1.4$, $\alpha_s = 0.5°$, $H = 10000$m, $\rho_\infty = 0.414$ kg / m^3, $c_\infty = 299.53$ m/s, $\hat{\tau} = 0.095$, $b = 0.5$ m, $a = -0.15$, $\omega_\xi = 86$ rad/s, $\omega_\alpha = 270$ rad/s, $\varpi = 0.32$, $\eta_\alpha = 10$, $\mu = 507.125$. The linear flutter speed is $U_L^* = 32.648$ and the Mach number, corresponding to linear flutter speed, is $M_L^* = 14.73$. We consider $V_r = U^*/U_L^*$ to be the velocity ratio.

The motion of the pitch was emphasized and the effect of the system parameters on the dynamics behaviour had been discussed comprehensively in Ref. [15]. So our study gives some result of both the pitch and plunge motion using the Poincaré map and Floquet theory. Moreover, we detect the effect of the initial conditions on the chaos of the system.

4.1. The Floquet multiplier of the Poincaré map

In this Subsection 4.1, the initial condition is always given to be $(\alpha, \dot{\alpha}, \xi, \dot{\xi})^{\mathrm{T}}|_{\tau=0} = (5°, 0, 0, 0)$ and the initial switch points are selected in the domain of convergence. By the Runge–Kutta numerical scheme, we obtained that if the flight speed in the domain $0 < V_r < 0.1677$, the trajectory converges to its equilibrium point $(0, 0, 0, 0)$. So we use the Poincaré map for the higher flight speed range $0.1677 \leq V_r \leq 1$.

The eigenvalue of the Jacobian matrix $\boldsymbol{DT}$ is taken to mean the Floquet multiplier. Based on the Floquet theory,[18,19] the cycle solution of the non-smooth dynamical system is stable if all the modules of the Floquet multipliers are less than 1. In contrast, the cycle solution is half-stable and the chaos will occur if one or more than one modulus is greater than or equal to 1 at the same time the other modules are all less than 1. The multiple cycle bifurcation occurs if one of the module bigger than or equal to 1 through -1.

We calculate Floquet multipliers and their modules for different V_r and some results are shown in Table 1. The Floquet multipliers given in Table 1 suggest the following facts: For the speed range $0.1677 \leq V_r < 0.2834$, the stable period-1 motion in pitch exists because the modules of the Floquet multipliers are all less than 1. At $V_r \approx 0.2834$, multiple cycle bifurcation occurs due to one of the Floquet multipliers is $\lambda_i \approx -1$. While at $0.2834 \leq V_r \leq 0.4254$, the system may exist complex dynamics behaviours, such as periodic, quasi-preiodic and chaotic behaviours. For example, one of the modulus of the Floquet multipliers is more than 1, so the chaos occur at $V_r = 0.2950$.[22] When the flight airspeed enhances to region $0.4254 < V_r < 1$, the pitch motion return to period-1 LCO again, but the amplitude of the LCO enhances contrast to that at the speed range $0.1677 \leq V_r < 0.2834$.

The above results are all highly consistent with the phase-plane diagrams in Fig. 4. Furthermore, at $V_r = 0.2950$, the largest or the top Lyapunov exponent[23–25] as shown in Fig. 5 is more than zero. This confirms the efficiency of the Floquet multipliers.

Table 1. The Floquet multiplier.

V_r	Floquet multiplier λ_i	modulus of Floquet multiplier $\lvert\lambda_i\rvert$
0.1702	$-0.70166 + 0.54744$	0.88997
	$-0.70166 - 0.54744$	0.88996
	0.96589	0.96589
0.2829	$0.27797 + 0.93472$i	0.97518
	$0.27797 - 0.93472$i	0.97518
	0.97708	0.97708
0.2832	$0.60621 + 0.61784$i	0.86557
	$0.60621 - 0.61784$i	0.86557
	-0.98497	0.98497
0.2834	$0.60634 + 0.61335$i	0.86247
	$0.606348 - 0.61335$i	0.86247
	-0.99034	0.99034
0.2950	$-0.21424 + 0.92526$i	0.94974
	$-0.21424 - 0.92526$i	0.94974
	1.00776	1.00776
0.8622	$-0.63520 + 0.67912$i	0.92989
	$-0.63520 - 0.679124$i	0.92989
	0.86326	0.86326

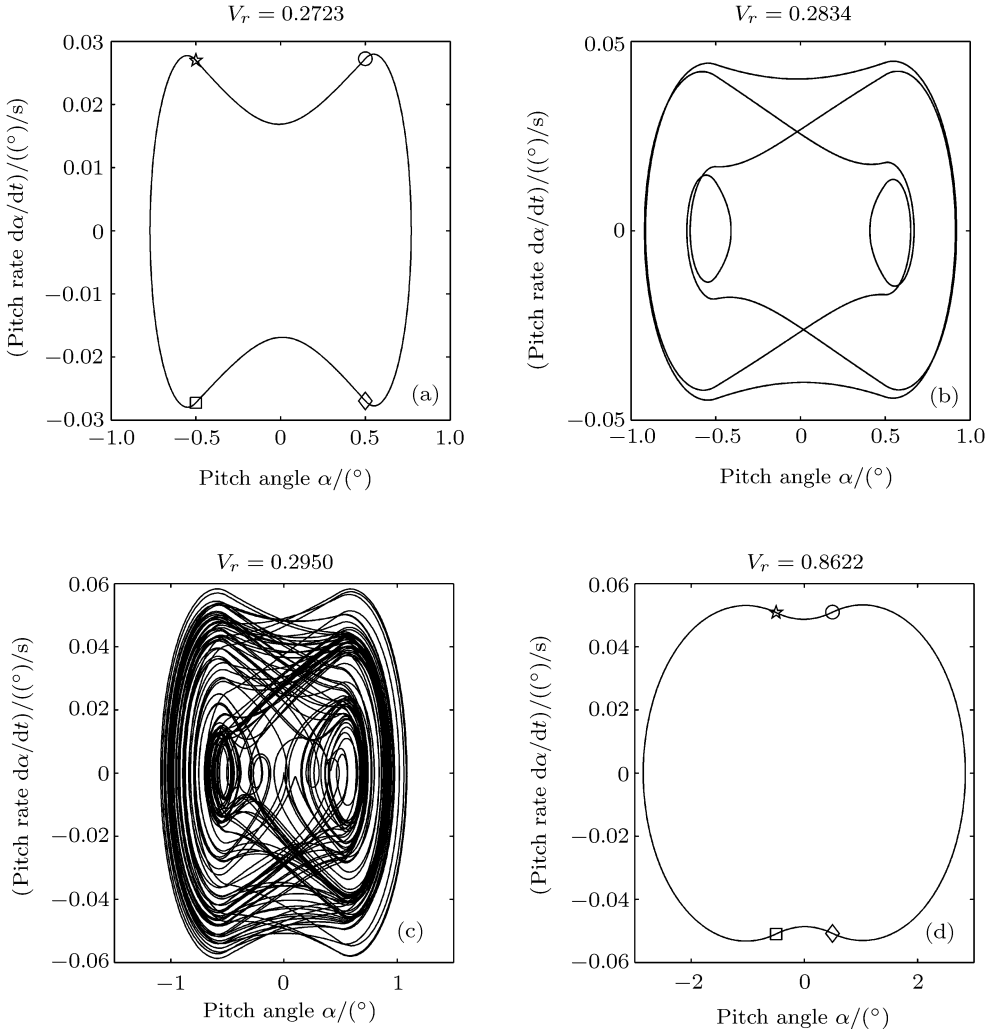


Fig. 4. The phase-plane figure of the pitch motion.

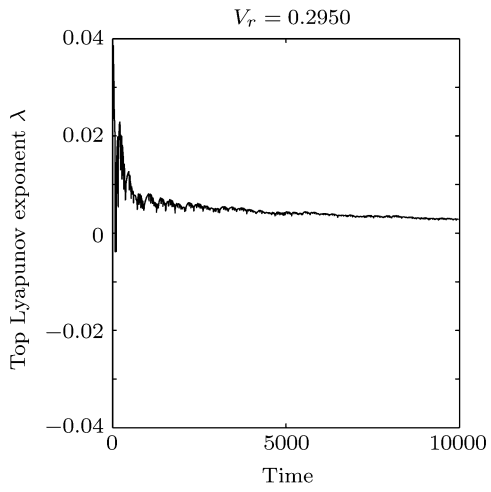


Fig. 5. The top Lyapunov exponent in the initial condition $(\alpha,\ \dot{\alpha},\ \xi,\ \dot{\xi})^{\mathrm{T}}\big|_{\tau=0} = (5^\circ, 0, 0, 0)$.

The plunge motion at different flight airspeed is given in Fig. 6. For $0.1677 \leq V_r < 0.2834$, the plunge motion which changes from periodic-1 to multi-periodic and then to periodic-1 motion again is more complex than the pitch motion. When $0.2834 \leq V_r \leq 0.4254$, the plunge behaviour is similar to that in pitch. Both the

multi-periodic and chaotic motion occur as shown in Figs. 6(f) and 6(g), and period-1 motion also exists in this region. While $0.4254 < V_r < 1$, the periodic-1 motion appears again as shown in Fig. 6(h).

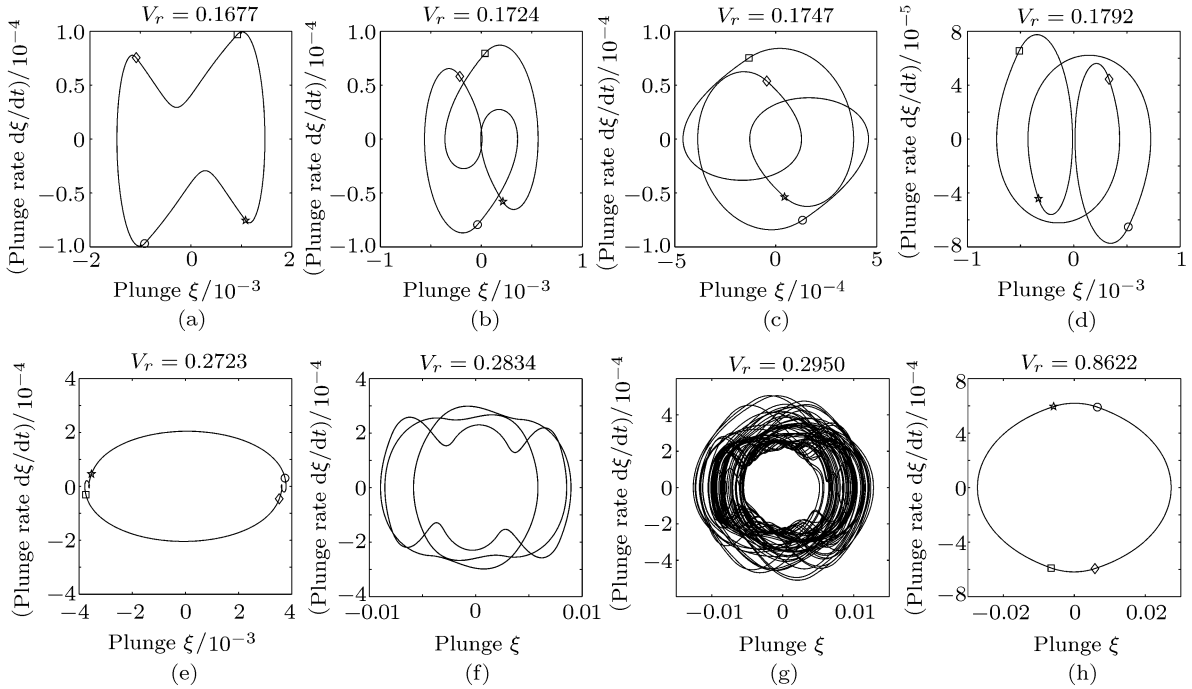


Fig. 6. The phase trajectory of the plunge motion.

4.2. The effect of the initial conditions

The dynamics behaviour of the system is sensitive to initial condition, especially in the airspeed region $0.2834 \leq V_r < 0.4254$. The chaos occurs in the system under some initial conditions, while periodic-1 or multi-periodic motion happens under other initial conditions. For example, at $V_r = 0.2950$ and $(\alpha, \dot{\alpha}, \xi, \dot{\xi})^{\mathrm{T}}|_{\tau=0} = (5^\circ, 0, 0, 0)$, the chaotic motion happens both in pitch and plunge as shown in Fig. 4(c) and Fig. 6(g). However, if the initial condition is $(\alpha, \dot{\alpha}, \xi, \dot{\xi})^{\mathrm{T}}|_{\tau=0} = (0.5^\circ, 0.03^\circ, 0, 0)$ and the other condition is same, the Floquet multiplies obtained are $-0.65275 + 0.64112\,\mathrm{i}, -0.65275 - 0.64112\,\mathrm{i}$ and 0.92639 and the stable periodic-1 motion exists as shown in Fig. 7.

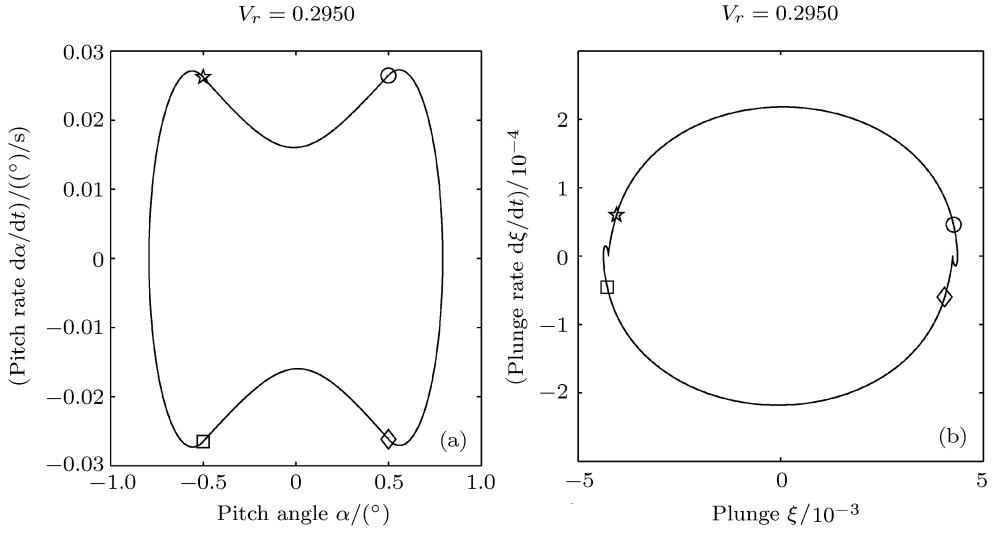


Fig. 7. The phase plane of the pitch and plunge motion when $(\alpha, \dot{\alpha}, \xi, \dot{\xi})^{\mathrm{T}}\big|_{\tau=0} = (0.5^\circ, 0.03^\circ, 0, 0)$. (a) pitch motion (b) plunge motion.

For the airspeed at $V_r = 0.2950$, we can demonstrate the phenomenon as followings: If the initial condition, such as $(\alpha, \dot{\alpha}, \xi, \dot{\xi})^{\mathrm{T}}\big|_{\tau=0} = (5^\circ, 0, 0, 0)$, locates nearby the saddle focus orbit, the horseshoes chaos appears. If the initial condition, $(\alpha, \dot{\alpha}, \xi, \dot{\xi})^{\mathrm{T}}\big|_{\tau=0} = (0.5^\circ, 0.03^\circ, 0, 0)$, locates nearby the periodic orbit, the trajectory converges to the LCO.

The Poincaré section[20] figures of the pitch rate, which crosses Π_0 in the positive direction as V_r increasing from 0.1677 to 1 under different initial condition, are shown in Fig. 8. They confirm some results in Subsection 4.1, especially the complex motion happened in the flight region $0.2834 \leq V_r \leq 0.4254$. It is also observed that the period-1 motion happens in the whole airspeed region at $(\alpha, \dot{\alpha}, \xi, \dot{\xi})^{\mathrm{T}}\big|_{\tau=0} = (0.5^\circ, 0.03^\circ, 0, 0)$ from Fig. 8(b). Contrasting Fig. 8(a) to Fig. 8(b), we obtain that the initial conditions have significant influence on the flight speed region $0.2834 \leq V_r \leq 0.4254$, and have little effect in the flight speeds regions $0.1677 \leq V_r < 0.2834$ and $0.4254 < V_r \leq 1$.

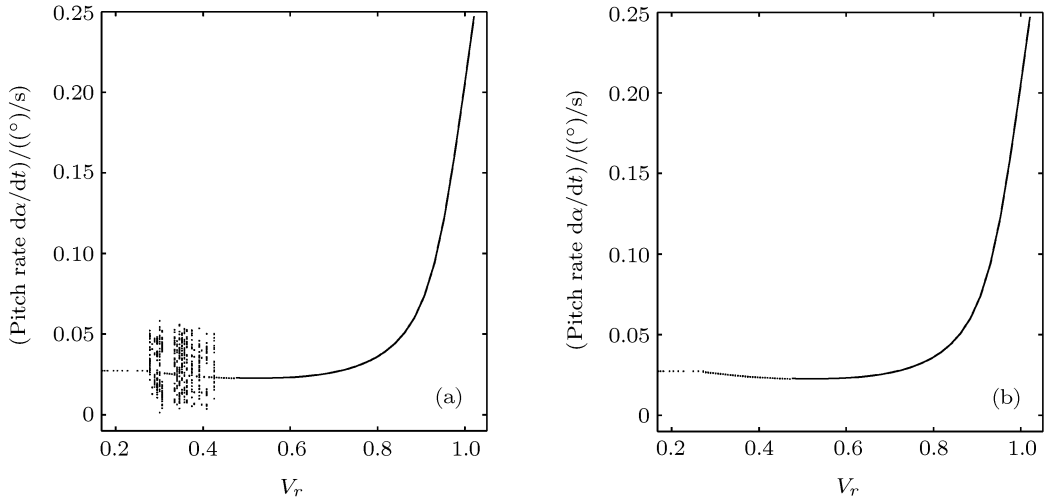


Fig. 8. The Poincaré section of the pitch rate in the initial condition (a) $(\alpha, \dot{\alpha}, \xi, \dot{\xi})^{\mathrm{T}}\big|_{\tau=0} = (5^\circ, 0, 0, 0)$ (b) $(\alpha, \dot{\alpha}, \xi, \dot{\xi})^{\mathrm{T}}\big|_{\tau=0} = (0.5^\circ, 0.03^\circ, 0, 0)$.

5. Conclusion

The paper studied the nonlinear aeroelastic airfoil with freeplay and cubic stiffness combined nonlinearities in pitch in the supersonic or hypersonic flight speed region. Using the Poincaré map method and Floquet theory, the dynamics behaviours including LCO, bifurcation and chaos are analysed and the primary results of the investigation can be summarized as follows.

Motion discipline of the pitch and plunge motion in increasing airspeed is derived. It reveals that under a certain initial condition, as the airspeed increases, the plunge motion turns out to be more complex than the pitch motion. It changes from a simple periodic-1 LCO to a multi-periodic motion and then to a periodic-1LCO again and then to chaos before finally changing back to periodic-1LCO.

Furthermore, the important effect of the initial condition on the system dynamics character is discussed in the paper. The trajectory with an initial condition located nearby the cycle orbit converges to the LCO, while with an initial condition located nearby the half-stabled saddle focus orbit leads to the chaos. The conclusion is also proved by the Floquet multiplier and the Poincaré section. Our achievement in this paper can provide important information for the control surface design of the airfoil. This method is capable of applying to study the piecewise-nonlinear dynamical system.

Appendix A

$\tau = U_\infty t/b$, $\xi = h/b$, $\chi_\alpha = S_\alpha/(mb)$, $r_\alpha^2 = I_\alpha/(mb^2)$, $\omega_\xi = \sqrt{K_h/m}$, $\omega_\alpha = \sqrt{K_\alpha/I_\alpha}$, $\zeta_h = c_h/2(K_h m)^{1/2}$, $\zeta_\alpha = c_\alpha/2(K_\alpha I_\alpha)^{1/2}$, $U^* = U/(b\omega_\alpha)$, $\bar{\omega} = \omega_\xi/\omega_\alpha$, $\mu = m/(4\rho_\infty b^2)$, $\hat{\tau} = t_h/b$.

Appendix B

$$\bar{\boldsymbol{M}} = \begin{bmatrix} 1 & \dfrac{\chi_\alpha}{r_\alpha^2} \\ \chi_\alpha & 1 \end{bmatrix}, \quad \bar{\boldsymbol{M}}^{-1} = \frac{1}{\chi_a^2 - r_a^2}\begin{bmatrix} -r_a^2 & \chi_\alpha \\ \chi_\alpha r_\alpha^2 & -r_a^2 \end{bmatrix}, \quad a_{21} = -\frac{(k_{21}\chi_a - k_{11}r_a^2)}{\chi_a^2 - r_a^2},$$

$$a_{22} = -\frac{(c_{21}\chi_a - c_{11}r_a^2)}{\chi_a^2 - r_a^2}, \quad a_{23} = -\frac{(k_{22}\chi_a - k_{12}r_a^2)}{\chi_a^2 - r_a^2}, \quad a_{24} = -\frac{(c_{22}\chi_a - c_{12}r_a^2)}{\chi_a^2 - r_a^2},$$

$$a_{41} = -\frac{(k_{11}\chi_a r_a^2 - k_{21}r_a^2)}{\chi_a^2 - r_a^2}, \quad a_{42} = -\frac{(c_{11}\chi_a r_a^2 - c_{21}r_a^2)}{\chi_a^2 - r_a^2}, \quad a_{43} = -\frac{(k_{12}\chi_a r_a^2 - k_{22}r_a^2)}{\chi_a^2 - r_a^2},$$

$$a_{44} = -\frac{(c_{12}\chi_a r_a^2 - c_{22}r_a^2)}{\chi_a^2 - r_a^2}, \quad f_1 = -\frac{\chi_a \bar{f}_2 - r_a^2 \bar{f}_1}{\chi_a^2 - r_a^2}, \quad f_2 = -\frac{\chi_a r_a^2 \bar{f}_1 - r_a^2 \bar{f}_2}{\chi_a^2 - r_a^2},$$

$$k_{11} = \left(\frac{1}{U^*}\right)^2(\bar{G}_a + 3\bar{G}_c\alpha_s^2) - \frac{\eta}{12M_\infty \mu r_\alpha^2}[12a + 3(r+1)\hat{\tau}\eta M_\infty + 3M_\infty^2(r+1)\hat{\tau}^2 a\eta^2]$$

$$k_{12} = 0, \quad k_{21} = \frac{\eta}{12M_\infty\mu}[-12a - 3(r+1)\hat{\tau}\eta M_\infty - 3M_\infty^2(r+1)\eta^2\hat{\tau}^2 a], \quad k_{22} = (\varpi/U^*)^2,$$

where M_∞ is the flight Mach number.

$$c_{11} = 2\frac{\xi_\alpha}{U^*} - \frac{\eta}{12M_\infty\mu r_\alpha^2}[-12(\frac{1}{3} + a^2) - 6a(r+1)\hat{\tau}\eta M_\infty - 3M_\infty^2(r+1)\eta^2\hat{\tau}a^2\eta^2 - M_\infty^2(r+1)\eta^2\hat{\tau}^2],$$

$$c_{12} = -\frac{\eta}{12M_\infty\mu r_\alpha^2}[12a + 3(r+1)\hat{\tau}\eta M_\infty + 3M_\infty^2\hat{\tau}^2(r+1)\eta^2 a],$$

$$c_{21} = \frac{\eta}{12M_\infty\mu}[-12a - 3(r+1)\hat{\tau}\eta M_\infty - 3M_\infty^2(r+1)\eta^2\hat{\tau}^2 a],$$

$$c_{22} = 2\xi_h\frac{\bar{\omega}}{U^*} + \frac{\eta}{12M_\infty\mu}[12 + 3M_\infty^2(r+1)\eta^2\hat{\tau}^2],$$

$$\bar{f}_1 = \left(\frac{1}{U^*}\right)^2\bar{G}_b + (\frac{1}{U^*})\bar{G}_c(\alpha^3 + 3*(-1)^n\alpha_s\alpha^2 + (-1)^n\alpha_s^3) - \frac{\eta}{12M_\infty\mu r_a^2}$$
$$\times\left[-M_\infty^2(r+1)\eta^2\left\{\frac{1}{5}\alpha'^3 - a(\xi' - a\alpha' + \alpha)^3 + \alpha'(\xi' - a\alpha' + \alpha)^2 - a\alpha'^2(\xi' - a\alpha' + \alpha)\right\}\right],$$

$$\bar{f}_2 = \frac{\eta}{12M_\infty\mu}M_\infty^2(r+1)\eta^2(\xi' - a\alpha' + \alpha)[(\xi' - a\alpha' + \alpha)^2 + \alpha'^2],$$

$$\bar{M}_{\mathrm{EA}}(\tau) = \frac{\eta}{12M_\infty\mu r_\alpha^2}\left[12\left[a\xi' - \left(\frac{1}{3} + a^2\right)\alpha' + a\alpha\right] + 3(\gamma+1)\hat{\tau}\eta M_\infty(\xi' - 2a\alpha' + \alpha)\right.$$
$$- M_\infty^2(\gamma+1)\eta^2\left\{\frac{1}{5}(\alpha')^3 - a(\xi' - a\alpha' + \alpha)\times[(\xi' - a\alpha' + \alpha)^2 + 3\hat{\tau}^2]\right.$$
$$\left.\left. + \alpha'[(\xi' - a\alpha' + \alpha)^2 + \hat{\tau}^2 - a\alpha'(\xi' - a\alpha' + \alpha)]\right\}\right],$$

$$\bar{L}(\tau) = -\frac{\eta}{12M_\infty\mu}[12(\xi' - a\alpha' + \alpha) - 3(\gamma+1)\hat{\tau}\eta M_\infty\alpha'$$
$$+ M_\infty^2(\gamma+1)\eta^2\{(\xi' - a\alpha' + \alpha)[(\xi' - a\alpha' + \alpha)^2 + 3\hat{\tau}^2 + (\alpha')^2]\}],$$

$$\bar{G}_a(\alpha)=\begin{cases}1, & \alpha(\tau)>\alpha_s;\\ 0, & -\alpha_s\le\alpha(\tau)\le\alpha_s;\\ 1, & \alpha(\tau)<\alpha_s.\end{cases};\quad \bar{G}_b(\alpha)=\begin{cases}-\alpha_s, & \alpha(\tau)>\alpha_s;\\ 0, & -\alpha_s\le\alpha(\tau)\le\alpha_s;\\ \alpha_s, & \alpha(\tau)<\alpha_s.\end{cases}$$

$$\bar{G}_a(\alpha)=\begin{cases}\hat{\eta}_\alpha(\alpha(\tau)-\alpha_s)^3, & \alpha(\tau)>\alpha_s;\\ 0, & -\alpha_s\le\alpha(\tau)\le\alpha_s;\\ \hat{\eta}_\alpha(\alpha(\tau)+\alpha_s)^3, & \alpha(\tau)<\alpha_s.\end{cases}$$

Nomenclature

a_h non-dimensional distance between elastic axis and mid-chord. b semi-chord. ξ non-dimensional plunging displacement at the elastic axis location ($\equiv h/b$). m airfoil mass per unit length. r_α non-dimensional radius of gyration ($\equiv\sqrt{I_\alpha/mb^2}$). ρ density of air. χ_α non-dimensional static unbalance about elastic axis. ζ_α,ζ_h pitch and heavy damping coefficients. α_s pitching freeplay magnitude. $\hat{\eta}_\alpha$ normalized nonlinear stiffness coefficient in pitching. x_α non-dimensional distance between elastic axis and centre of mass. K_α,K_ξ pitch and plunge stiffness coefficients. α,ξ airfoil motion in pitch and plunge (heavy) direction. U,U^* velocity and its non-dimension counterpart(reduced velocity), ($\equiv U_\infty/b\omega_\alpha$), respectively. $\omega_\alpha,\omega_h,\varpi$ uncoupled frequency in plunging and pitching, and non-dimension frequency ratio, respectively. μ reduced mass ratio, ($\equiv m/4\rho_\infty b^2$). c_∞ speed of sound. M_∞ Mach number ($\equiv U_\infty/c_\infty$). t,τ physical time variable and non-dimensional time ($\equiv U_{\rm m}t/b$), respectively. ($\dot{}$), ($\ddot{}$) First and second time derivatives. ( )′, ( )″ first- and second-derivative with respect to non-dimensional time. $L(t)$, $M_{\rm EA}$ lift force and aerodynamic moment about the elastic axis. $M(\theta)$ freeplay nonlinear storing force model. M_0, M_f,θ_f,δ are freeplay nonlinearity parameters.

References

[1] Lee B H K, Price S J and Wong Y S 1999 *Prog. Aerosp. Sci.* **35** 205

[2] Raghothama A and Narayanan S 1999 *J. Sound Vib.* **226** 493

[3] Liu L P and Dowell E H 2004 *Nonlinear Dyn.* **37** 31

[4] Zhang Q C, Liu H Y and Ren A D 2004 *Tianjin Daxue Xuebao* **22** 614 (in Chinese)

[5] Chen Y M and Liu J K 2007 *Journal of Aerospace Power* **22** 614 (in Chinese)

[6] Liu L, Wong Y S and Lee B H K 2000 *J. Sound Vib.* **234** 641

[7] Liu L, Wong Y S and Lee B H K 2002 *J. Sound Vib.* **253** 447

[8] Chung K W, He Y B and Lee B H K 2009 *J. Sound Vib.* **320** 163

[9] Chung K W, Chan C L and Lee B H K 2007 *J. Sound Vib.* **299** 520

[10] Zhao Y H and Hu H Y 2003 *Hangkong Xuebao* **24** 521 (in Chinese)

[11] Yu M L and Hu H Y 2005 *J. Vibrat. Engin.* **18** 418 (in Chinese)

[12] Yu M L, Wen H and Hu H Y 2006 *J. Vibrat. Engin.* **19** 326 (in Chinese)

[13] Yu M L, Wen H, Hu H Y and Zhao Y H 2007 *Hangkong Xuebao* **28** 340 (in Chinese)

[14] Gu Y S and Yang Z C 2008 *Adv. Mater. Res.* **33-37** 1247

[15] Abbas L K, Chen Q, O'Donnell K, Valentine D and Marzocca P 2007 *Aerosp. Sci. Technol.* **11** 405

[16] HU H Y 1995 *Chaos, Solitons and Fractals* **5** 2201

[17] Wang Q Y, Lu Q S and Wang H X 2005 *Chin. Phys.* **14** 2189

[18] Lu Q S and Jin L 2005 *Acta Mechanica Solida Sinica* **26** 132 (in Chinese)

[19] Jin L, Lu Q S and Wang Q 2004 *Yingyong Lixue Xuebao* **21** 21 (in Chinese)

[20] Thomas S. Parker, Leon O and Chua Practical 1989 *Numerical Algorithms for Chaotic Systems* (Berlin: Springer)

[21] Brandon Q, Ueta T, Fournier-prunaret D and Kousaka T 2009 *Chaos, Solitons and Fractals* **42** 187

[22] Silva C P 1993 *IEEE Trans. Circuits-1* **40** 675

[23] Müller P C 1995 *Chaos, Solitons and Fractals* **5** 1671

[24] Jin L and Lu Q S 2005 *Acta. Mech. Sin.* **37** 40 (in Chinese)

[25] Yang J J, Li J, Deng X Z and Fang Z D 2008 *Mechanical Science and Technology for Aerospace Engineering* **27** 728 (in Chinese)